

A holistic structural understanding of epitaxially-grown Bi/Au(111) moiré superstructures

Pablo Vezzoni Vicente¹, Tobias Weiss¹, Dennis Meier¹, Wenchao Zhao¹, Sena Tömekçe¹, Marc G. Cuxart^{1,2}, Benedikt P. Klein^{3,4}, David A. Duncan³, Tien-Lin Lee³, Anthoula C. Papageorgiou^{1,6}, Matthias Muntwiler⁵, Ari Paavo Seitsonen⁷, Willi Auwärter¹, Peter Feulner¹, Johannes V. Barth¹, and Francesco Allegretti^{1,*}

¹Physics Department E20, TUM School of Natural Sciences, Technical University of Munich, 85748 Garching, Germany

²Institut Català de Nanociència i Nanotecnologia, 08193 Bellaterra, Spain

³Diamond Light Source, Harwell Science and Innovation Campus, Didcot OX11 0DE, United Kingdom

⁴Department of Chemistry, University of Warwick, Coventry CV4 7AL, United Kingdom

⁵Photon Science Division, Paul Scherrer Institut, Villigen 5232, Switzerland

⁶Department of Chemistry, National and Kapodistrian University of Athens, Panepistimiopolis 15771 Athens, Greece

⁷Department of Chemistry, École Normale Supérieure, 75005 Paris, France

*francesco.allegretti@tum.de

July 16, 2024

Abstract

In light of the recent research interest in low-dimensional bismuth structures as spin-active materials and topological insulators, we present a comprehensive characterisation of the Bi/Au(111) interface. The nuanced evolution of Bi phases upon deposition in ultra-high vacuum (UHV) on a Au(111) surface is investigated from semi-disordered clusters to few-layer Bi(110) thin films. Particular attention is devoted to the high-coverage, sub-monolayer phases, commonly grouped under the $(P \times \sqrt{3})$ nomenclature. We bring forth a new model, refining the current understanding of the Bi/Au(111) interface and demonstrating the existence of sub-monolayer moiré superstructures, whose geometry and superperiodicity depend on their coverage. This tuneable periodicity paves the way for their use as tailored buffer and templating layers for epitaxial growth of thin films on Au(111). Finally, we clarify the growth mode of multilayer Bi(110) as bilayer-by-bilayer, allowing precise thickness control of anisotropically-strained thin films. This holistic understanding of the structural properties of the material was enabled by the synergy of several experimental techniques, namely low-energy electron diffraction (LEED), X-ray photoelectron spectroscopy (XPS), scanning tunnelling microscopy and spectroscopy (STM, STS), and X-ray standing waves (XSW), further corroborated by density functional theory (DFT) simulations.

1 Introduction

As the heaviest naturally-occurring pnictogen, an element belonging to the periodic table's group V, bismuth has been extensively studied due to its particularly large spin-orbit interaction [1, 2], which is of distinct relevance for spintronic applications such as room-temperature quantum spin Hall materials [3, 4]. Two-dimensional Bi sheets, commonly called bismuthene, are predicted to be topological insulators due to the presence of non-trivial edge states [5, 6]. Likewise, thin-film Bi(111) and Bi(110) layers have been reported as potential topologically active materials, with tuneable properties depending on the number of layers [1, 5]. Attempts at epitaxial growth in ultra-high vacuum (UHV) have already been performed on several substrates [7, 8, 9, 10], including a recent report of flat bismuthene on SiC(0001) [11, 12], whereas a tendency towards the formation of surface alloys has been highlighted on coinage metals [13, 14, 15, 16],

which are common substrates for *in-vacuo* epitaxy.

On Au(111), several studies describe a wide array of ordered phases obtained by electrochemical deposition at the liquid-solid interface: (2×2) , $(P \times \sqrt{3})$, $(7 \times 7)R21.8^\circ$, and $(5 \times 25\sqrt{3}/3)$ [17, 18, 19], which likely became of interest in light of the emergent catalytic activity of Bi-decorated gold surfaces [20]. Nevertheless, only a handful of studies have explored the complex succession of phases that occurs upon Bi deposition in UHV [21, 22, 23]. Most significantly, the existing literature presents conflicting results on some of the finer details, revealing an incomplete understanding of the structural properties of the different Bi phases. For example, the low-coverage (6×6) phase observed by Jeon et al. [21] was later refined as a $(\sqrt{37} \times \sqrt{37})R25.3^\circ$ Kagome lattice, while both layer-by-layer (Frank-van der Merwe) [22] and island (Stranski-Krastanov) [23] growth modes have been reported for the multilayer.

Lastly, promising results have been achieved using

the Bi-functionalised Au(111) surface as a template layer for molecular deposition [24], whereas the multilayer growth of weakly-interacting Bi(110) bilayer films on gold [22, 23] suggests the potential use as a buffer layer, when direct interaction of other adsorbates with the substrate is undesirable. For instance, recent examples of single-atom magnets with unprecedented stability [25] and 2D polymers produced by photopolymerisation [26] emphasise the relevance of rationally-chosen buffer layers.

In this paper, we refer to the low-coverage, sub-monolayer Bi/Au(111) phase as a benchmark to identify the optimal growth conditions for Bi thin films. Utilising a suite of experimental techniques, namely low-energy electron diffraction (LEED), X-ray photoelectron spectroscopy (XPS), scanning tunneling microscopy and spectroscopy (STM, STS), and X-ray standing waves (XSW), we present a holistic understanding of the $(P \times \sqrt{3})$ phase’s structure [22, 23]. In contrast to the reports of incommensurability, we report a succession of high-coverage, sub-monolayer phases with slightly different lattice parameters that yield a series of moiré superstructures of increasing superperiodicity, confirmed by our density functional theory (DFT) simulations. Finally, we rely on STM and LEED measurements, as well as our newly-developed model, to understand the multilayer growth mode and rationalise the formation of Bi(110) thin films.

2 Experimental Methods

Preliminary tests to identify the ideal deposition conditions were conducted at TUM Physics E20 in a UHV chamber with a base pressure better than 1×10^{-10} mbar, housing LEED optics, a SPECS Phoibos 100 CCD electron energy analyser, and a custom-built X-ray gun with an Al/Mg dual anode. High-resolution XPS (HR-XPS) data, LEED patterns enhanced by a microchannel-plate (MCP) detector, and normal-incidence X-ray standing waves (NIXSW) profiles were then recorded at the I09 beamline of the Diamond Light Source in Didcot (United Kingdom) [27], where two undulators allow the simultaneous irradiation of the sample with soft (0.1–2.0 keV) and hard (2.1–20 keV) X-rays. Scanning probe experiments (STM, STS) were conducted at TUM Physics E20 in a chamber with base pressure better than 2×10^{-10} mbar, equipped with a CreaTec low-temperature STM setup capable of cooling down to 6 K, as well as at the PEARL endstation of the Swiss Light Source (SLS) synchrotron in Villigen (Switzerland), equipped with an Omicron LT-STM apparatus capable of cooling down to 4 K. The LEED setups at E20 and I09 are OCI Vacuum Microengineering Inc. LEED optics, whereas the electron energy analysers at PEARL and I09 are VG Scienta EW4000 and EW4000 HAXPES respectively. The LEED measurements were performed at sample temperatures between 300 K and 80 K. No changes were observed as a function of temperature for any of the phases other than a sharpening of the

diffraction spots on colder samples due to the reduced background noise. Both the LT-STM chamber at E20 and the PEARL endstation are also equipped with LEED optics, used to ensure a consistent quality of the grown samples across all experimental chambers.

The Au(111) samples were cleaned by repeated cycles of sputtering with Ar^+ or Ne^+ and annealing at 725 K for 5 min. Bi deposition was performed in UHV by heating a MaTeck granulate of 99.999% purity through a custom-built evaporator and controlling the temperature through a thermocouple attached directly to the granulate-containing crucible. The evaporation temperature was kept at 750 K. The details regarding the calibration of the adsorbate coverage are presented in the Supplemental Material (SM), Section S1 [28]. In this work, we define 1 ML as the coverage at which the whole surface is covered by an atomically-thin Bi sheet, beyond which any excess Bi triggers multilayer growth. All presented XPS spectra were fitted with a convolution of Gaussian and Doniach-Sunjic lineshapes while subtracting a combination of constant, linear, and Shirley backgrounds [29, 30]. The STM data was analysed using WSxM 4.0 and SpmImage Tycoon [31, 32]. In STM height profiles, a calibration factor of 0.92 along the vertical direction was determined using the known height of the Au step. Kinematically simulated LEED patterns were produced using LEEDpat 4.2 [33]. The presented structural models were rendered using VESTA 3 [34].

The DFT [35] calculations were performed using the codes Quantum ESPRESSO (QE) [36] and Vienna Ab-initio Simulation Package (VASP) [37]. The exchange-correlation term in the Kohn-Sham Hamiltonian was approximated with the generalised gradient approximation by Perdew, Burke and Ernzerhof [38]. Using QE, the equilibrium lattice constant of Au was determined to be 4.1469 Å, and this value was thus used in subsequent calculations. However, when quantitatively comparing the DFT results with experimental data, a 0.9834 correction factor was applied to the simulated distances to account for the Au lattice constant being larger than the 4.0782 Å experimental value [39]. The Bi-Au interface was modelled as a slab consisting of five layers of Au and a terminating layer of hydrogen atoms at the bottom in order to accelerate the convergence of the electronic structure toward the solution at thicker slabs. The two top layers of the Au(111) slab were allowed to relax in all three directions and the terminating H vertically at the face centred cubic (FCC) adsorption sites; convergence was concluded when the energy changed less than 10^{-9} eV. The $(P \times \sqrt{3})$ structures were simulated based on the experimentally-developed model hereafter. Spin-orbit coupling was not included in the calculations, as it is expected to have little effect on the geometry. The lateral Brillouin zone was sampled with an equidistance grid of $n \times 12$ k points, where $n = 4, 4, 2, 2, 2$ as $P = 5, 8, 11, 14, 17$. We used a Fermi-Dirac broadening of the occupation numbers with a width of 50 meV. The discontinuity of the electrostatic potential in the

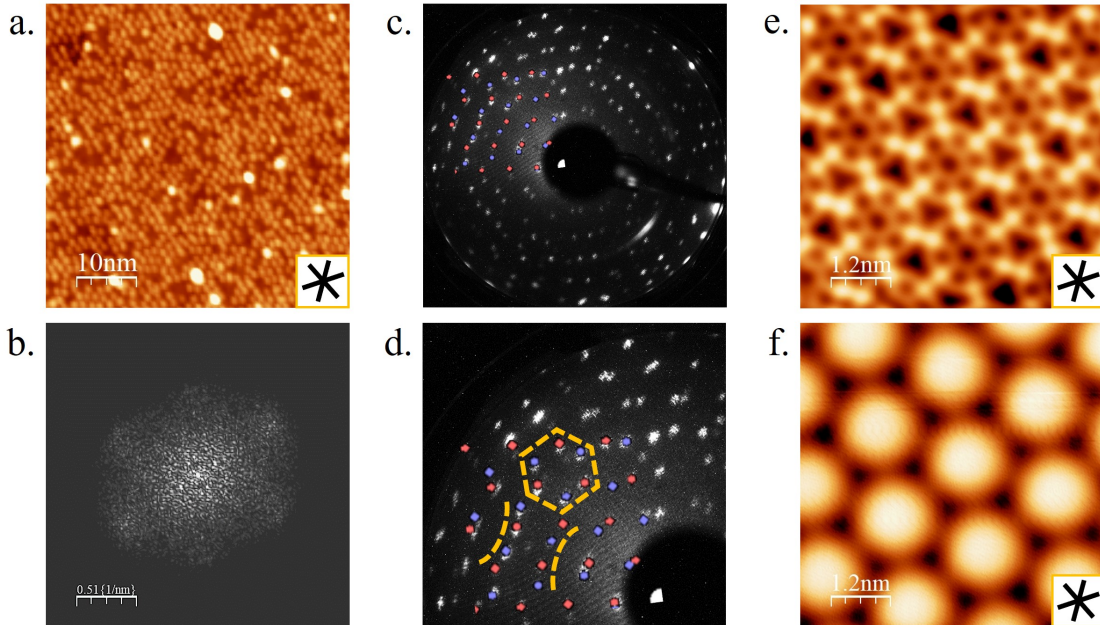


Figure 1: (a) Low-Temperature STM image ($V=1.00$ V, $I=34$ pA) of very-low-coverage Bi/Au, showing disordered clusters. (b) Fourier-transformed image of panel a. (c) LEED pattern of the low-coverage ($\sqrt{37} \times \sqrt{37}$) $R25.3^\circ$ phase, with the corresponding simulated pattern superimposed (red and blue spots correspond to different symmetry domains). (d) Zoomed-in image of panel c, highlighting (yellow) some characteristic features of the LEED pattern, demonstrating the agreement between experimental and simulated data. (e) STM image ($V=-0.01$ V, $I=100$ pA) of the low-coverage phase. (f) STM image ($V=2.50$ V, $I=100$ pA) of the same area as in panel e.

vacuum was ensured with the surface dipole correction. The Bi core-level binding energies were evaluated by shifting half of an electron from the chosen core level to the Fermi energy.

3 Results and Discussion

3.1 The Low-Coverage Systems

At very-low coverage (< 0.5 ML), the adsorbed Bi atoms aggregate into clusters (Figure 1a), which have recently been the subject of increasing research interest [40]. While seemingly disordered, a weak tendency of the clusters to arrange following the hexagonal surface layer’s symmetry of the substrate is evidenced by the 2D fast Fourier transform (FFT) of the STM data (Figure 1b). Both results agree with the literature reports of a poor-quality (5×5) cluster arrangement at ≈ 5 K [22, 23]. Jeon et al. observed the clusters to be highly mobile at room temperature (RT) [21], as confirmed by the lack of a LEED pattern beyond that of the underlying Au(111) substrate (not shown), in accordance with the results by He et al. [23].

As the coverage increases (≈ 0.57 ML), an ordered phase appears with ($\sqrt{37} \times \sqrt{37}$) $R25.3^\circ$ symmetry, which is in line with previous literature reports [22, 23] and indicates the correct reproduction of the expected Bi/Au(111) systems. This phase will be further referred to as the “low-coverage phase” to distinguish it from the high-coverage striped phases that occur upon further Bi deposition up to completion of the monolayer. Its characteristic LEED pattern is presented in

Figure 1c (cf. details in Figure 1d), while a typical STM image is shown in Figure 1e and images at larger tip-bias voltage are reported in Figures 1e and S2 [28], expanding the currently available literature.

3.2 The ($P \times \sqrt{3}$) Phase

A further phase transition occurs at a coverage of ≈ 0.81 ML, as the six-fold symmetric ($\sqrt{37} \times \sqrt{37}$) $R25.3^\circ$ phase transforms into a two-fold symmetric high-coverage, sub-ML structure. The latter is known as the ($P \times \sqrt{3}$) phase [22, 23], a nomenclature used in the literature and referring to its commensurate $\sqrt{3}$ periodicity along the substrate’s $[11\bar{2}]$ direction and incommensurate P periodicity perpendicular to it, which gradually decreases as the coverage increases. A characteristic striped pattern was observed in our LT-STM measurements upon further Bi deposition (Figure 2a), with stripes aligned along the $[11\bar{2}]$ direction of the Au(111) substrate and an apparent height modulation occurring perpendicularly to the stripes’ axis (Figure 2b). The transition from the low-coverage phase to a ($P \times \sqrt{3}$) structure is evident from the distinct changes in STM topography (Figures 1e and 2a) and LEED pattern (Figures 1c and 3a). Here, the sub-ML coverage is confirmed by comparison of the STS spectrum in Figure 2c with the ones reported by Kawakami et al., where the lack of features other than a shoulder around 0.7 V was associated with the monolayer regime [22], as well as by the coverage calibration presented in Section S1 [28].

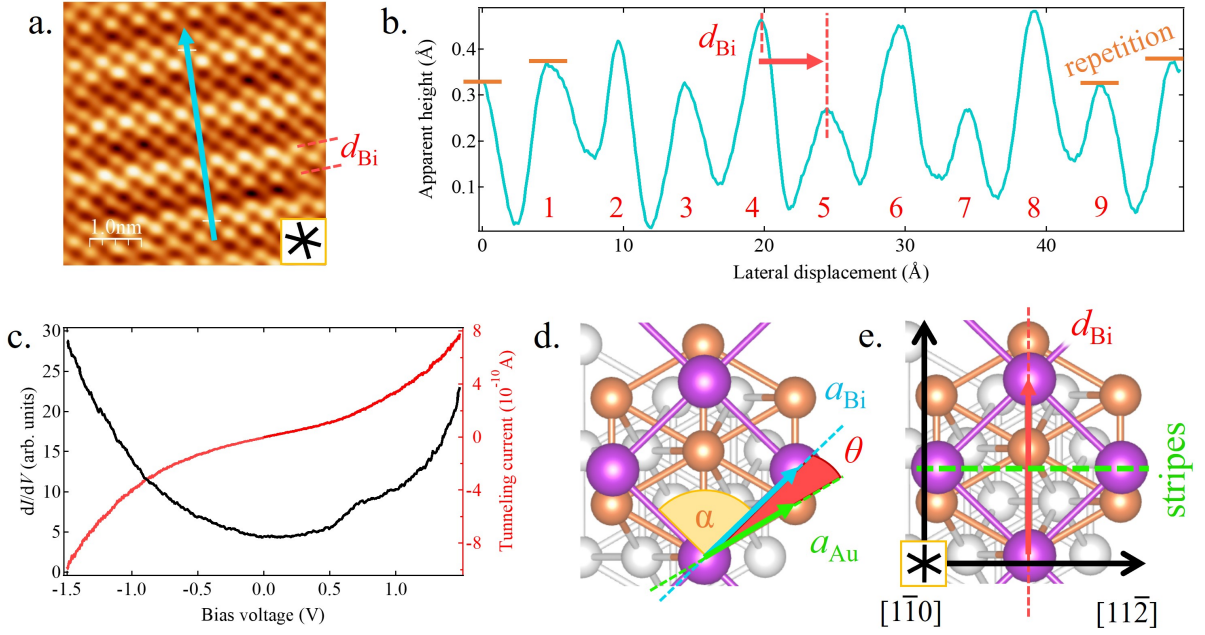


Figure 2: (a) Low-Temperature STM image of high-coverage Bi/Au ($V=0.10$ V, $I=500$ pA). The Fourier-transformed image was filtered to reduce the noise contribution. (b) Height profile along the azure arrow drawn in panel a. The red numbers highlight a change in relief across neighbouring stripes. (c) Typical STS spectrum recorded on the structure in panel a. (d) Depiction of the rotation and size of the Bi unit cell (purple) relative to that of the topmost Au layer (orange). The rotation angle between the two unit cells amounts to $\theta=12.5^\circ$, defined by the Bi and Au lattice vectors (respectively, a_{Bi} and a_{Au}), while the angle between the Bi lattice vectors is $\alpha=95^\circ$ (thus $\alpha/27\theta=60^\circ$). Note that the Bi atom used as reference to build the unit cell has here been arbitrarily placed in a top adsorption site to facilitate the understanding of the symmetry relation. (e) Highlight on the image from panel d of the direction of the stripes observed in panel a, aligned along the $[1\bar{1}2]$ substrate direction. In this work, we use the letters a and b to indicate the lattice vectors, l for the nearest neighbour distance, d for the diagonals, and $*$ to distinguish the moiré supercell from the unit cell.

The bismuth adlayer arranges into a nearly-square lattice, with lattice vectors 1.16 times longer than the substrate's and a lattice angle of 95° . The Bi unit cell is rotated by 12.5° relative to that of the underlying Au(111), thus aligning its diagonals along the substrate's $[1\bar{1}0]$ and $[11\bar{2}]$ directions respectively (Figure 2d). We therefore introduce the notation of $(1.16 \times 1.16)R12.5^\circ A95^\circ$ for this and similar structures. The periodicity along the stripes is $\approx 5 \text{ \AA}$, compatible with $\sqrt{3} l_{\text{Au}}$ ($l_{\text{Au}} = 2.88 \text{ \AA}$), which is commensurate along the substrate's $[11\bar{2}]$ direction (Figure 2e). The spacing between adjacent stripes appears to be $2|d_{\text{Bi}}| = 8.85 \text{ \AA} = 3.07 l_{\text{Au}}$. However, the imperfect periodicity of the apparent height profile across neighbouring stripes, indicated in Figure 2b, suggests the presence of a longer-range superperiodicity perpendicularly to the stripes. In fact, the alignment of d_{Bi} parallel to the $[1\bar{1}0]$ direction of the Au(111) surface entails the possibility of a long-range moiré coincidence between the Bi superlattice and the substrate along this direction. This would signify that the Bi superstructure's unit cell in this direction spans multiple stripes, in contrast with the claims of incommensurability advanced in the literature [22, 23].

It has been reported in the literature that the

$(P \times \sqrt{3})$ phase is characterised by the superstructure's periodicity perpendicular to the stripes (P) shrinking as the coverage increases [23], resulting in a succession of incommensurate superstructures on the surface [22]. Nevertheless, we find this to not be compatible with the observed LEED patterns (Figure S5) [28] and propose instead a succession of commensurate moiré patterns of increasing superperiodicity arising as the coverage increases up to 1 ML. As evident from Figure 3a, this complex system produces an intricate LEED pattern, whose coverage dependence is most conveniently observed in six "shrinking triangles" (green), named after the tendency of the six spots contained in each of them to grow closer together at increasing coverages.

We propose the structural model in Figure 3b, in which the stripes develop along the substrate's $[11\bar{2}]$ direction with constant periodicity, $|a_{\text{Bi}}^*| = \sqrt{3} l_{\text{Au}}$ (the $*$ distinguishing the lattice parameters of the rectangular supercell from those of the nearly-square unit cell). In order to maintain this periodicity as the coverage increases, the nearest neighbour distance of the high-coverage Bi phase ($|a_{\text{Bi}}| = |b_{\text{Bi}}| = l_{\text{Bi}}$) gradually decreases, as does the rotation angle (θ) relative to the Au(111) unit-cell vectors, whereas the

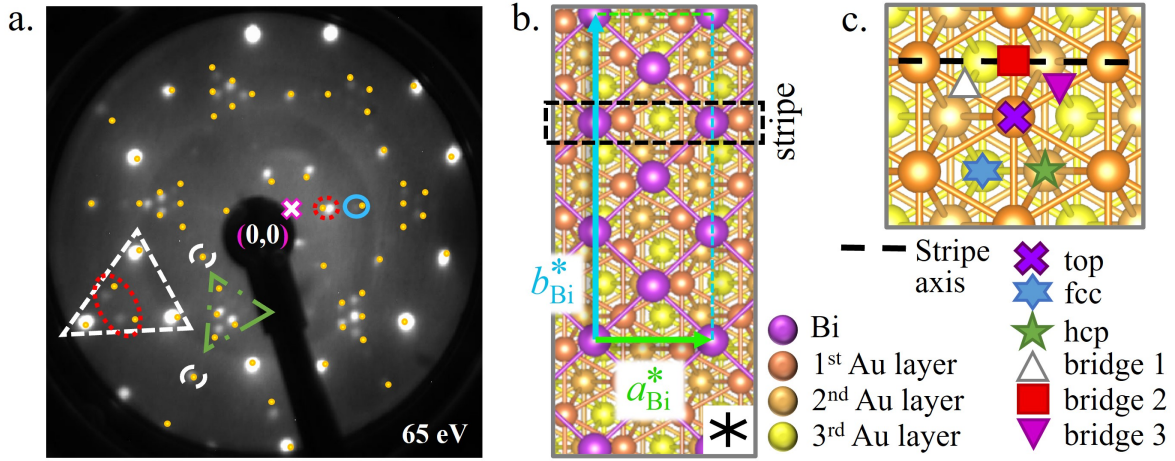


Figure 3: LEED pattern of the $(P \times \sqrt{3})$ phase at a coverage of ≈ 1 ML, on which are superimposed the dots (yellow) of an analogous phase of lower coverage (Figure S3b) [28]. Highlighted are some spots which exhibit different trends as the coverage increases: stationary (white, dashed), moving away from the (0,0) spot (red, dotted), approaching the (0,0) spot (blue, full), and a “shrinking triangle” (green, dash-dotted). (b) Structural model of the $(5 \times \sqrt{3})$ superstructure, on which are highlighted the Bi supercell’s lattice vectors parallel (a_{Bi}^*) and perpendicular (b_{Bi}^*) to the striped pattern in Figure 2a. The direction of the stripes is highlighted in black. Models of the longer-periodicity moiré structures are displayed in Figure S4 [28]. (c) High-symmetry adsorption sites on the Au(111) surface. The bridge sites are differentiated to account for their orientation relative to the moiré supercell: at $\pm 30^\circ$ angles with the stripe axis for “bridge 1” and “bridge 3” positions, and perpendicular to the stripe axis for the “bridge 2” site.

angle (α) between the Bi unit-cell vectors increases (defined in Figure 2d). As a result, the length of the Bi unit cell’s diagonal perpendicular to the stripes (d_{Bi}) is reduced. This, however, does not cause the superstructure’s lattice constant in this direction (b_{Bi}^*) to shrink, which would lead to an incommensurate adlayer. Instead, b_{Bi}^* spans a greater number of d_{Bi} units, reaching a commensurate moiré periodicity over a larger scale (Figure S4).

In order to obtain further structural information regarding the adlayer, we conducted normal-incidence XSW measurements (see Section S3.1). The fitted NIXSW data and the resulting coherent parameters (f coherent fraction, p coherent position) are reported in Figure 4c. Relative to the surface reflection ((111) planes), the high coherent fraction indicates a markedly flat layer, and therefore that the adsorption height can be derived from the coherent position (assuming a negligible surface relaxation of the substrate). As the period of the standing wave matches the planar spacing of the crystal along the [111] direction (2.35 Å), there are multiple adsorption heights that mathematically agree with our measured results, the so-called “modulo- d ” [41]. Excluding any negative (Bi intercalation) or unphysically large values, only heights of 0.19 Å, 2.54 Å or 4.89 Å would agree with our experimentally measured p_{111} values (Figure 4a-b). The correct adsorption height can be determined by means of triangulation, recording the NIXSW profiles relative to non-equivalent planes, tilted with respect to the surface plane (Figure 4c), and comparing the experimental results with the coherent parameters of

a simulated structure (Figure 4a: $(\bar{1}11)$ planes, Figure 4b: (200) planes). Further details of our NIXSW triangulation analysis are presented in Section S3.1. We infer the correct value to be $h_{\text{Au}}^{\text{Bi}} = 2.54 \pm 0.03$ Å, slightly exceeding the substrate’s spacing but significantly smaller than the planar spacing of Bi(110) ($h_{\text{Bi}}^{110} = 3.28$ Å). Furthermore, triangulation allows the identification of the lateral adsorption sites, as the coherent parameters are strongly dependent on the geometry within the unit cell of the simulated structure. The three-fold rotational symmetry of the Au(111) surface, and therefore the presence of three rotational domains for high-coverage Bi, is taken into account in the simulated NIXSW data by introducing rotationally-equivalent reflection planes (i.e. $(\bar{1}\bar{1}1)$ and $(11\bar{1})$ for the $(\bar{1}11)$ reflection or (020) and (002) for the (200) reflection). It is found that a “reference atom” must be placed in a bridge position not aligned perpendicularly to the stripes’ direction (Figure 3c, “bridge 1” or “bridge 3”), while the rest of the structure is determined through the observations made above (Figure S6). Consequently, all Bi atoms are either found in bridge sites at 30° from the $\sqrt{3}$ direction of the moiré supercell (a_{Bi}^* in Figure 3b), e.g. the surface’s $[11\bar{2}]$ direction, or in intermediate positions between two such sites, excluding any other high-symmetry adsorption sites.

It should be noted that the NIXSW measurements were conducted at room temperature and under the exposure to intense X-ray beams. In order to account for thermal effects, the atomic positions of the simulated flat adsorbate structure were modified by

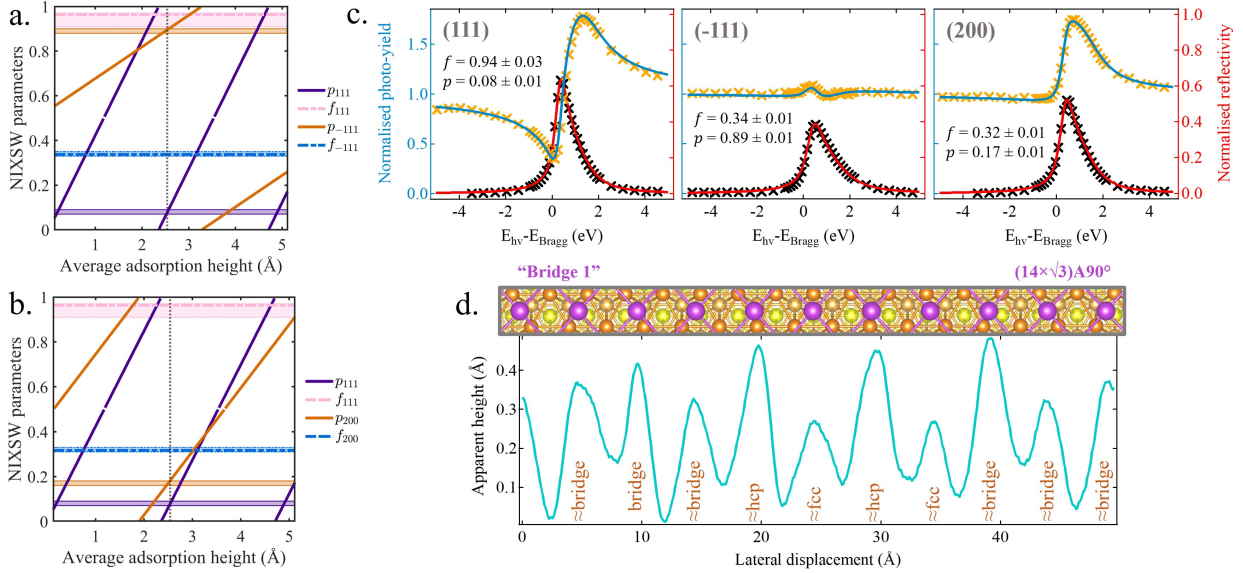


Figure 4: Simulated coherent fraction and position plotted as a function of the adsorption height, referring to the $(11 \times \sqrt{3})A90^\circ$ moiré superstructure, modified to account for structural disorder. The colour-shaded areas indicate the value range measured experimentally for each parameter, and the dotted vertical line highlights the adsorption value of 2.54 \AA , for which simulation and experiment agree (overlap) in all proposed moiré superstructures. The coherent values relative to the (111) reflection are compared to those relative to: (a) the $(\bar{1}\bar{1}1)$ reflection, (b) the (200) reflection. (c) Experimental NIXSW data markers (orange: photo-yield, black: reflectivity) and fitting curves (blue and red respectively) for high-coverage Bi/Au(111) and all measured reflection planes. The coherent parameters obtained from the fits are listed in each image. (d) Graphical comparison of the adsorption sites in the “bridge 1” $(14 \times \sqrt{3})A90^\circ$ superstructure (above) with the topographic profile measured by STM in Figure 3a (below). The approximate adsorption sites deduced from the model are written in orange. The colour scheme of the structural model is defined in Figure 3b.

introducing a Gaussian distribution with standard deviation of 0.10 \AA along the Cartesian axis perpendicular to the surface (z) as well as 0.05 \AA along the two axes parallel to it (x, y). For a perfectly flat adsorbate layer, the coherent fraction relative to the surface reflection (here, (111)) should be 1. Considering that the experimental value is affected by both static (defects) and dynamic disorder (thermal movement) as well as by any mosaicity of the substrate’s surface, we consider the measured $f_{111} = 0.94 \pm 0.03$ to be highly consistent with the formation of a markedly flat layer. The different adsorption sites of the Bi atoms within the moiré supercells only result in a minor corrugation, compatible with the $\approx 0.2 \text{ \AA}$ differences in apparent height measured by STM (Figure 4c). The triangulation plots of the ideal simulated structure, prior to the introduction of the aforementioned Gaussian deviations, are presented in Figure S7 alongside those of the other high-symmetry sites, whose exclusion is discussed in Section S3 [28].

Only one dissonant note occurs in the analysis here presented, reported in Figure 4d. As shown, the STM height profile perpendicular to the stripe axis does not match the expected corrugation for the “bridge 1” $(14 \times \sqrt{3})A90^\circ$ phase, assuming the adsorption height in bridge sites to be larger than in intermediate positions (closer to hcp and fcc sites). A better correspondence is found when placing the

reference atom in a “bridge 2” site (Figure S7f) [28], defined in Figure 3c. Nevertheless, this is in conflict with the NIXSW triangulation analysis, which clearly excludes this bridge position as a feasible adsorption site (Figure S7e) [28]. This effect is tentatively attributed to the fact that the STM topographic signal does not correspond to the structural geometry, but to its convolution with the local density of states. Alternatively, the assumption made in Figure 4d of the adsorption height being lower on bridge sites than at intermediate positions may not be correct for this system.

Despite this discrepancy, additional evidence in favour of the “bridge 1” model arises from density functional theory (DFT) calculations. Allowing relaxation of the $(n \times \sqrt{3})A90^\circ$ supercells ($n = 5, 8, 11, 14, 17$), yields structures whose geometry and adsorption sites well match the proposed models (cf. Figure 5a-b). Moreover, the respective average adsorption heights range from 2.50 \AA to 2.58 \AA in good agreement with the 2.54 \AA extracted from the NIXSW data (Figure 5c). In fact, while most values lie just outside of the calculated $\pm 0.03 \text{ \AA}$ margin of error, deviations between experiment and theory of 0.11 \AA are generally considered in excellent agreement [42].

The experimentally measured HR-XPS spectra can be fitted with a single component for the Bi $4f_{7/2}$ core level (centered at a binding energy of 156.9 eV), despite

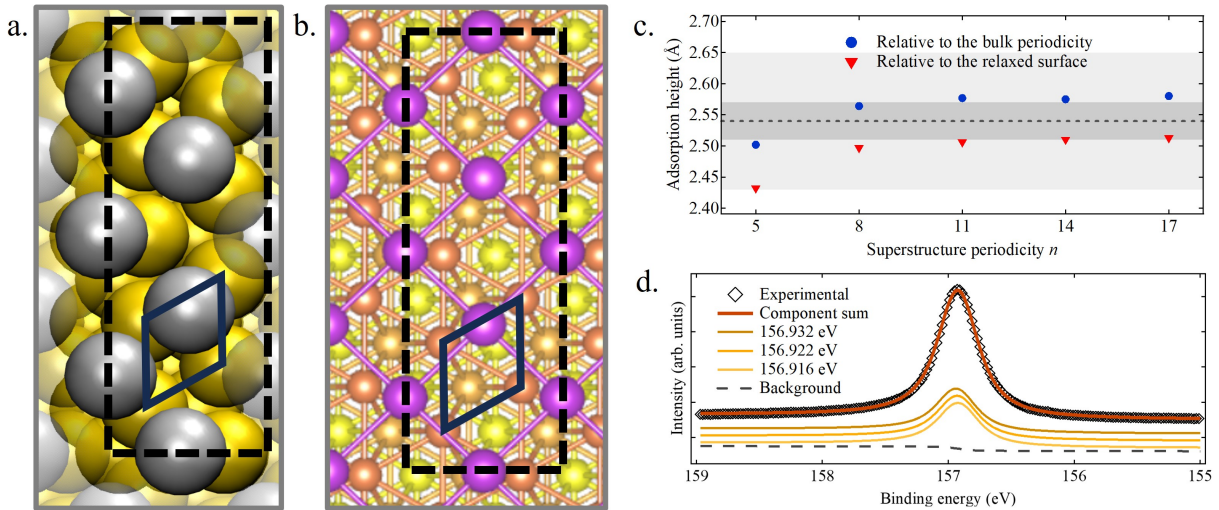


Figure 5: (a) DFT-simulated $(5 \times \sqrt{3})A90^\circ$ superstructure, displaying the adsorption sites of the relaxed Bi layer (grey) on the Au(111) substrate (yellow). (b) Model used for the simulation of XSW parameters for the $(5 \times \sqrt{3})A90^\circ$ superstructure, with colour scheme as in Figure 3b. The unit cells of the topmost Au(111) layer (blue) and the Bi superstructure (black, dashed) are highlighted to facilitate the comparison with panel a. (c) Adsorption heights of the $(n \times \sqrt{3})A90^\circ$ superstructures as calculated by DFT (blue circles: with respect planes maintaining the bulk periodicity; red triangles: with respect to the surface layer), compared to the value measured by XSW (dotted line, uncertainty given as a dark grey shading). The light grey shading visualises a deviation within $\pm 0.11 \text{ \AA}$ from the latter value. (d) Comparison of the HR-XPS Bi $4f_{7/2}$ core-level spectrum (beamline I09, photon energy 275 eV) with components binding energies calculated by DFT for the $(5 \times \sqrt{3})A90^\circ$ superstructure (three values, each corresponding to two Bi atoms), homogeneously shifted to align with the experimental spectrum (-6.31 eV from the absolute value of the simulation). Arbitrary vertical shifts have been applied to facilitate the visualisation.

the high resolution achieved as synchrotron facilities, indicating similar chemical environments for all Bi atoms within the supercell (Figure 5d). Our DFT calculations yield a spread in binding energy of 0.016 eV for atoms in different adsorption sites, well within the experimental resolution, thus justifying the appearance of a single peak. Alongside the small shift of the Bi $4f_{7/2}$ core level from its bulk value of 157 eV [43], this hints to a weak charge transfer between substrate and adsorbate, suggesting similar bonding as within a Bi(110) bilayer and therefore its potential applications as a decoupling layer.

3.3 The Multilayer Regime

Despite a general consensus in the literature that Bi(110) grows in the multilayer regime, He et al. observe a Stranski-Krastanov growth mode of bilayer ribbons on top of the high-coverage phase [23], whereas Kawakami et al. report a Frank-Van der Merwe growth mode for the first few layers which turns into an island growth mode around 12 ML [22]. We believe the multilayer to begin growing upon saturation of the $(14 \times \sqrt{3})A90^\circ$ superstructure in the monolayer, whose unit cell closely resembles that of Bi(110) with a 4.8% expansion along the $[11\bar{2}]$ direction and a 1.1% compression along the $[1\bar{1}0]$ direction [44, 45, 46]. Given the negligible change of the LEED pattern during thin-film growth, the coverage calibration was performed using HR-XPS measurements. The areas of the Bi $4f_{7/2}$ XPS core levels from multilayer samples were

compared to references at known coverage. Samples of 1.54 ML and 2.14 ML coverage were prepared and measured in STM at $\approx 4 \text{ K}$ following deposition at 300 K as well as after annealing at 450 K for 10 min. In both cases, rather large and homogeneous terraces of the high-coverage phase with the occasional appearance of ribbon-like islands were observed, not unlike those reported by He et al. [23] (Figure 6a). We find bilayer-Bi steps (height: 6.7 \AA) to be much more common than single-layer ones. Moreover, as shown in Figure S8a-b, single-layer steps (3.3 \AA) can be ascribed to the edge of growing bilayers. We therefore consider the formation of odd-numbered layers, including the first Bi layer at the interface, to be the preferential growth mode.

The latter observation may be justified by the tendency of few-ML Bi to saturate any dangling bonds, arranging into energetically-favoured Bi(110) bilayers (Figure S9) [44, 8]. Given that STM indicates the formation of a monolayer of Bi on Au(111), which does not contribute to the formation of Bi(110) bilayers in the multilayer regime, we postulate that the first Bi layer saturates its bonds by interaction with the Au substrate, which prospectively the high-coverage system as an effective buffer layer for the epitaxial growth of further adsorbates [24]. Along this line of research, we report a strong decoupling action upon phosphorus deposition (Figure 6c). HR-XPS shows a milder shift in binding energy of the P $2p_{3/2}$ core level from the bulk black P value (129.9 eV) [43] when adsorbed on Bi/Au(111) (129.60 eV) than in the P/Au(111) system

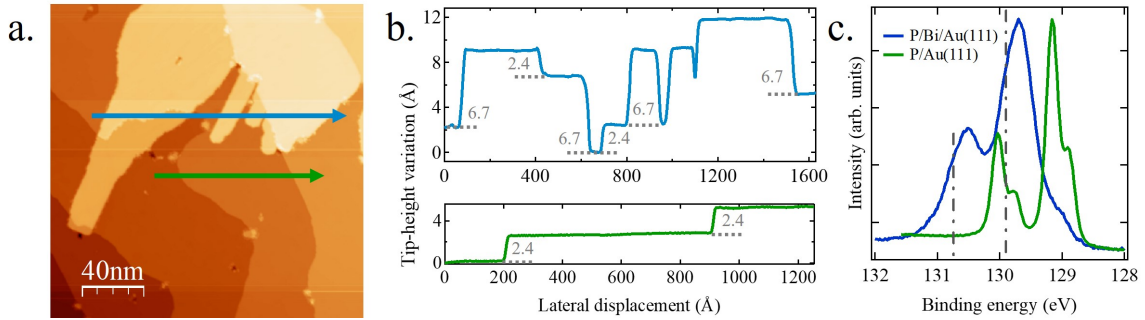


Figure 6: (a) STM image of a 2.14 ML Bi thin film on Au(111) ($V=1.00$ V, $I=10$ pA). The blue (top) and green (bottom) arrows indicate the paths along which the height profiles in panel b were taken. (b) Height profiles from panel a, highlighting the commonly-seen Au single steps (2.4 Å) and Bi(100) bilayer islands (6.7 Å). (c) HR-XPS P $2p$ core levels of P on high-coverage Bi/Au (blue, left) and P/Au (green, right), measured at the I09 and PEARL beamlines and respectively (photon energies: 275 eV and 210 eV). The dotted grey lines indicate the binding energies and relative intensities of the P $2p_{1/2}$ (left) and P $2p_{3/2}$ (right) peaks in bulk black phosphorus [43].

(129.16 eV, for the largest component). A broadening of the spectrum is also observed and assigned to the varied, largely disordered adsorption configurations of P on the functionalised surface, as indicated by the unaltered LEED pattern relative to that of clean, high-coverage Bi/Au(111) (not shown). Significantly, no change in the lineshape of the Bi $4f_{7/2}$ XPS spectrum was observed upon P deposition (Figure S8c), despite the high resolution achieved through synchrotron radiation, suggesting a weak electronic interaction of the Bi/Au(111) system with the additional adsorbate.

4 Conclusions

In conclusion, we present an extensive characterisation of the diverse phases obtained by deposition of Bi onto a Au(111) surface in UHV: from disordered clusters at very-low coverage (< 0.5 ML) to the multilayer regime (≈ 2 ML). Contrary to previous reports, we do not find the so-called ($P \times \sqrt{3}$) phase ($0.8 - 1$ ML) to be incommensurate and characterised by its shrinking lattice parameter (P) as the coverage increases. Instead, four discrete moiré superstructures of increasing periodicity form by encompassing a larger number of unit cells, which we called the $(n \times \sqrt{3})A90^\circ$ phases ($n = 5, 8, 11, 14$; $A90^\circ$ indicating the 90° angle between the supercell’s lattice vectors). Their electronic decoupling effect on post-deposited adsorbates is demonstrated through P deposition, which, alongside the tuneable geometry and moiré patterning, supports their use as buffer layers for epitaxial growth on Au(111). Finally, we report the stabilisation of the $(14 \times \sqrt{3})A90^\circ$ superstructure as the system transitions into the multilayer regime, due to the close resemblance of this structure with Bi(110), stretched by 4.8% along the substrate’s $[11\bar{2}]$ direction and compressed by 1.1% along the $[\bar{1}\bar{1}0]$ direction. The preferential growth occurs through the formation of bilayers, which allow to minimise the presence of dangling bonds, while each bilayer tends to be completed before the onset of the following one. We expect the

weakly interacting, mildly strained bilayers to be of interest for further research on Bi(110) thin films and their topologically non-trivial properties.

Acknowledgements

The authors gratefully recognise the technical assistance and experimental support of Karl Eberle, Dave McCue and Patrick Ascher, respectively at the Technical University of Munich, Diamond Light Source, and the Paul Scherrer Institut. This work was financially supported by the Deutsche Forschungsgemeinschaft (DFG, German Research Foundation) under the Clusters of Excellence (ExStra) program, project EXC-2089/1-390776260 (e-conversion). We acknowledge the Diamond Light Source for provision of synchrotron beamtime (SI25907-2) as well as the priority program COORNETs (SPP1928) with project number 316890188. M.G.C. acknowledges funding from the European Union’s Horizon 2020 Research and Innovation Programme under the Marie Skłodowska-Curie grant agreement no. 892725 (WHITEMAG project). The authors declare no conflict of interest.

References

- [1] E. Aktürk, O. Ü. Aktürk, and S. Ciraci, “Single and bilayer bismuthene: stability at high temperature and mechanical and electronic properties,” *Physical Review B*, vol. 94, no. 1, p. 014115, 2016.
- [2] C. R. Ast, J. Henk, A. Ernst, L. Moreschini, M. C. Falub, D. Pacilé, P. Bruno, K. Kern, and M. Gironi, “Giant spin splitting through surface alloying,” *Physical Review Letters*, vol. 98, no. 18, p. 186807, 2007.
- [3] S. Murakami, “Quantum spin hall effect and enhanced magnetic response by spin-orbit coupling,” *Physical Review Letters*, vol. 97, no. 23, pp. 1–4, 2006.

- [4] C. Sabater, D. Gosálbez-Martínez, J. Fernández-Rossier, J. G. Rodrigo, C. Untiedt, and J. J. Palacios, “Topologically protected quantum transport in locally exfoliated bismuth at room temperature,” *Physical Review Letters*, vol. 110, no. 17, p. 176802, 2013.
- [5] Z. Liu, C. X. Liu, Y. S. Wu, W. H. Duan, F. Liu, and J. Wu, “Stable nontrivial Z_2 topology in ultrathin Bi (111) films: a first-principles study,” *Physical Review Letters*, vol. 107, no. 13, p. 136805, 2011.
- [6] M. Wada, S. Murakami, F. Freimuth, and G. Bihlmayer, “Localized edge states in two-dimensional topological insulators: Ultrathin Bi films,” *Physical Review B - Condensed Matter and Materials Physics*, vol. 83, no. 12, pp. 2–5, 2011.
- [7] R. H. Miwa, T. M. Schmidt, and G. P. Srivastava, “Bi covered Si(111) surface revisited,” *Journal of Physics Condensed Matter*, vol. 15, no. 17, pp. 2441–2447, 2003.
- [8] T. Nagao, J. T. Sadowski, M. Saito, S. Yaginuma, Y. Fujikawa, T. Kogure, T. Ohno, Y. Hasegawa, S. Hasegawa, and T. Sakurai, “Nanofilm allotrope and phase transformation of ultrathin Bi film on Si(111)- 7×7 ,” *Physical Review Letters*, vol. 93, no. 10, pp. 10–13, 2004.
- [9] J. Cui, M. Daboczi, M. Regue, Y.-C. Chin, K. Pagano, J. Zhang, M. Isaacs, G. Kerverve, A. Mornto, J. West, S. Gimenez, J.-S. Kim, and S. Eslava, “Two-Dimensional Bismuthene as a Functional Interlayer between BiVO_4 and NiFeOOH for Enhanced Oxygen-Evolution Photoanodes,” *Advanced Functional Materials*, vol. 32, p. 2207136, 2022.
- [10] Y. Liu, S. Benter, C. S. Ong, R. P. Maciel, A. Irish, O. Eriksson, A. Mikkelsen, and R. Timm, “A 2D Bismuth-Induced Honeycomb Surface Structure on GaAs(111),” *ACS Nano*, vol. 17, no. 5, pp. 5047–5058, 2023.
- [11] F. Reis, G. Li, L. Dudy, M. Bauernfeind, S. Glass, W. Hanke, R. Thomale, J. Schäfer, and R. Claessen, “Bismuthene on a SiC substrate: a candidate for a high-temperature quantum spin Hall material,” *Science*, vol. 357, pp. 287–290, 2017.
- [12] C. H. Hsu, Z. Q. Huang, F. C. Chuang, C. C. Kuo, Y. T. Liu, H. Lin, and A. Bansil, “The nontrivial electronic structure of Bi/Sb honeycombs on SiC(0001),” *New Journal of Physics*, vol. 17, p. 025005, 2015.
- [13] Y. Girard, C. Chacon, G. De Abreu, J. Lagoute, V. Repain, and S. Rousset, “Growth of Bi on Cu(111): alloying and dealloying transitions,” *Surface Science*, vol. 617, pp. 118–123, 2013.
- [14] C. Kato, Y. Aoki, and H. Hirayama, “Scanning tunneling microscopy of Bi-induced Ag(111) surface structures,” *Physical Review B - Condensed Matter and Materials Physics*, vol. 82, no. 16, p. 165407, 2010.
- [15] K. H. Zhang, I. M. McLeod, M. Lahti, K. Pussi, and V. R. Dhanak, “The evolution of the electronic structure at the Bi/Ag(111) interface studied using photoemission spectroscopy,” *Journal of Physics Condensed Matter*, vol. 24, no. 43, p. 435502, 2012.
- [16] K. H. Zhang, I. M. McLeod, Y. H. Lu, V. R. Dhanak, A. Matilainen, M. Lahti, K. Pussi, R. G. Egdell, X. S. Wang, A. T. Wee, and W. Chen, “Observation of a surface alloying-to-dealloying transition during growth of Bi on Ag(111),” *Physical Review B - Condensed Matter and Materials Physics*, vol. 83, no. 23, p. 235418, 2011.
- [17] C.-h. Chen, K. D. Kepler, A. A. Gewirth, B. M. Ocko, and J. Wang, “Electrodeposited Bismuth Monolayers on Au(111) Electrodes: Comparison of Surface X-ray Scattering, Scanning Tunneling Microscopy, and Atomic Force Microscopy Lattice Structures,” *Journal of Physical Chemistry*, vol. 97, pp. 7290–7294, 1993.
- [18] K. Tamura, J. X. Wang, R. R. Adzic, and B. M. Ocko, “Kinetics of Monolayer Bi Electrodeposition on Au(111): Surface X-ray Scattering and Current Transients,” *Journal of Physical Chemistry B*, vol. 108, no. 6, pp. 1992–1998, 2004.
- [19] Y. C. Fu, Y. Z. Su, H. M. Zhang, J. W. Yan, Z. X. Xie, and B. W. Mao, “An in situ scanning tunneling microscopic study of electrodeposition of bismuth on Au(1 1 1) in a 1-butyl-3-methylimidazolium tetrafluoroborate ionic liquid: Precursor adsorption and underpotential deposition,” *Electrochimica Acta*, vol. 55, no. 27, pp. 8105–8110, 2010.
- [20] M. Nakamura, N. Sato, N. Hoshi, and O. Sakata, “Catalytically active structure of Bi deposited on a Au(111) electrode for the hydrogen peroxide reduction reaction,” *Langmuir*, vol. 26, no. 7, pp. 4590–4593, 2010.
- [21] J. H. Jeon, K. H. Chung, H. Kim, and S. J. Kahng, “Corner hole adatom stacking fault structure of Bi on Au(1 1 1),” *Surface Science*, vol. 603, no. 1, pp. 145–150, 2009.
- [22] N. Kawakami, C. L. Lin, K. Kawahara, M. Kawai, R. Arafune, and N. Takagi, “Structural evolution of Bi thin films on Au(111) revealed by scanning tunneling microscopy,” *Physical Review B*, vol. 96, no. 20, p. 205402, 2017.
- [23] B. He, G. Tian, J. Gou, B. Liu, K. Shen, Q. Tian, Z. Yu, F. Song, H. Xie, Y. Gao, Y. Lu, K. Wu, L. Chen, and H. Huang, “Structural and electronic properties of atomically thin bismuth on

- Au(111),” *Surface Science*, vol. 679, pp. 147–153, 2019.
- [24] G. Tian, Y. Shen, B. He, Z. Yu, F. Song, Y. Lu, P. Wang, Y. Gao, and H. Huang, “Effects of monolayer Bi on the self-assembly of DBBA on Au(111),” *Surface Science*, vol. 665, no. 111, pp. 89–95, 2017.
- [25] F. Donati, S. Rusponi, S. Stepanow, C. Wäckerlin, A. Singha, L. Persichetti, R. Baltic, K. Diller, F. Patthey, E. Fernandes, J. Dreiser, Šljivančanin, K. Kummer, C. Nistor, P. Gambardella, and H. Brune, “Magnetic remanence in single atoms,” *Science*, vol. 352, no. 6283, pp. 318–321, 2016.
- [26] L. Grossmann, B. T. King, S. Reichlmaier, N. Hartmann, J. Rosen, W. M. Heckl, J. Björk, and M. Lackinger, “On-surface photopolymerization of two-dimensional polymers ordered on the mesoscale,” *Nature Chemistry*, vol. 13, no. 8, pp. 730–736, 2021.
- [27] T. L. Lee and D. A. Duncan, “A Two-Color Beamline for Electron Spectroscopies at Diamond Light Source,” *Synchrotron Radiation News*, vol. 31, no. 4, pp. 16–22, 2018.
- [28] See Supplemental Material at <https://thelinkofthepaper.com> for the coverage calibration, the details of the NIXSW analysis, and other supporting figures.
- [29] G. H. Major, N. Fairley, P. M. A. Sherwood, M. R. Linford, J. Terry, V. Fernandez, and K. Artyushkova, “Practical guide for curve fitting in X-ray photoelectron spectroscopy,” *Journal of Vacuum Science Technology A*, vol. 38, no. 6, p. 061203, 2020.
- [30] M. H. Engelhard, D. R. Baer, A. Herrera-Gomez, and P. M. A. Sherwood, “Introductory guide to backgrounds in XPS spectra and their impact on determining peak intensities,” *Journal of Vacuum Science Technology A*, vol. 38, no. 6, p. 063203, 2020.
- [31] A. Riss, “Spmimage tycoon: Organize and analyze scanning probe microscopy data,” *Journal of Open Source Software*, vol. 7, no. 77, p. 4644, 2022.
- [32] I. Horcas, R. Fernández, J. M. Gómez-Rodríguez, J. Colchero, J. Gómez-Herrero, and A. M. Baro, “WSXM: A software for scanning probe microscopy and a tool for nanotechnology,” *Review of Scientific Instruments*, vol. 78, no. 1, p. 013705, 2007.
- [33] K. Hermann and M. A. V. Hove, “Software utility LEEDpat (version 4.2),” *Berlin/Hong Kong*, 2015.
- [34] K. Momma and F. Izumi, “VESTA3 for three-dimensional visualization of crystal, volumetric and morphology data,” *Journal of Applied Crystallography*, vol. 44, no. 6, pp. 1272–1276, 2011.
- [35] P. Hohenberg and W. Kohn, “Inhomogeneous Electron Gas,” *Physical Review*, vol. 136, no. 3B, p. B864, 1964.
- [36] P. Giannozzi, S. Baroni, N. Bonini, M. Calandra, R. Car, C. Cavazzoni, D. Ceresoli, G. L. Chiarotti, M. Cococcioni, I. Dabo, A. Dal Corso, S. De Gironcoli, S. Fabris, G. Fratesi, R. Gebauer, U. Gerstmann, C. Gougousis, A. Kokalj, M. Lazzeri, L. Martin-Samos, N. Marzari, F. Mauri, R. Mazzarello, S. Paolini, A. Pasquarello, L. Paulatto, C. Sbraccia, S. Scandolo, G. Sclauzero, A. P. Seitsonen, A. Smogunov, P. Umari, and R. M. Wentzcovitch, “QUANTUM ESPRESSO: A modular and open-source software project for quantum simulations of materials,” *Journal of Physics Condensed Matter*, vol. 21, no. 39, 2009.
- [37] G. Kresse and J. Furthmüller, “Efficient iterative schemes for ab initio total-energy calculations using a plane-wave basis set,” *Physical Review B*, vol. 54, no. 16, p. 11169, 1996.
- [38] J. P. Perdew, K. Burke, and M. Ernzerhof, “Generalized Gradient Approximation Made Simple,” *Physical Review Letters*, vol. 77, no. 18, pp. 3865–3868, 1996.
- [39] A. Maeland and T. B. Flanagan, “Lattice spacings of gold-palladium alloys,” *Canadian Journal of Physics*, vol. 42, pp. 2364–2366, 1964.
- [40] F. Pan, B. Peerless, and S. Dehnen, “Bismuth-Based Metal Clusters From Molecular Aesthetics to Contemporary Materials Science,” *Accounts of Chemical Research*, vol. 56, no. 9, pp. 1018–1030, 2023.
- [41] J. Zegenhagen and A. Kazimirov, *The X-Ray Standing Wave Technique*. World Scientific, 2013.
- [42] B. P. Klein, M. A. Stoodley, D. B. Morgan, L. A. Rochford, L. B. Williams, P. T. Ryan, L. Sattler, S. M. Weber, G. Hilt, T. J. Liddy, T. L. Lee, R. J. Maurer, and D. A. Duncan, “Probing the role of surface termination in the adsorption of azupyrene on copper,” *Nanoscale*, vol. 16, pp. 5802–5812, 2024.
- [43] J. F. Moulder, W. F. Stickle, P. E. Sobol, and K. D. Bomben, *Handbook of X-ray Photoelectron Spectroscopy*. Perkin-Elmer Corporation, 1992.
- [44] G. Bian, X. Wang, T. Miller, T. C. Chiang, P. J. Kowalczyk, O. Mahapatra, and S. A. Brown, “First-principles and spectroscopic studies of Bi(110) films: Thickness-dependent Dirac modes and property oscillations,” *Physical Review B - Condensed Matter and Materials Physics*, vol. 90, no. 19, p. 195409, 2014.
- [45] F. He, E. S. Walker, and Y. Zhou, “Phase transition in epitaxial bismuth nanofilms,” *Applied Physics Letters*, vol. 117, p. 073103, 2020.

- [46] M. Jankowski, D. Kamiński, K. Vergeer, M. Mirolo, F. Carla, G. Rijnders, and T. R. Bollmann, “Controlling the growth of Bi(110) and Bi(111) films on an insulating substrate,” *Nanotechnology*, vol. 28, no. 15, 2017.
- [47] B. W. Batterman, “Effect of dynamical diffraction in x-ray fluorescence scattering,” *Physical Review*, vol. 133, no. 3A, pp. A759–A764, 1964.
- [48] J. Als-Nielsen and D. McMorrow, *Elements of Modern X-ray Physics*. Wiley, 2011.
- [49] D. P. Woodruff, “Surface structure determination using x-ray standing waves,” *Reports on Progress in Physics*, vol. 68, no. 4, pp. 743–798, 2005.
- [50] J. Zegenhagen, “Surface structure determination with X-ray standing waves,” *Surface Science Reports*, vol. 18, pp. 199–271, 1993.
- [51] P. Hofmann, “The surfaces of bismuth: Structural and electronic properties,” *Progress in Surface Science*, vol. 81, no. 5, pp. 191–245, 2006.

A holistic structural understanding of epitaxially-grown Bi/Au(111) moiré superstructures

Supplemental Material

S1 Coverage calibration

The reproduction of the desired bismuth structure could be confirmed by comparison of the obtained LEED patterns (Figure S1a-c) with those reported by He et al. [23]. The changing P parameter in the $(P \times \sqrt{3})$ phase is reflected in a set of spots arranged into a triangle, highlighted in Figure S1c, which appears to gradually shrink as the coverage increases (cf. Figure S1c-d). We assign the onset of the multilayer growth to the coverage for which the LEED pattern ceases to mutate (cf. Figure S1d-e), despite further Bi deposition being reflected in the increased intensity of the XPS signal. Assuming the sticking coefficient of Bi to remain constant during deposition up to 1 ML, the deposition times can be used as a metric of the coverage by comparing the observed LEED patterns to the literature [23] and relying on the reported coverages. The obtained results are summarised in table S1. Further evidence of the transitions between different phases comes from the NIXSW data, in which a small increase in coherent fraction can be seen upon the transition from the low-coverage to the high-coverage phase (from 0.81 to 0.94, corresponding to Figure S1a-c respectively), whereas a sharp drop is measured upon formation of a multilayer (to 0.49, Figure S1e).

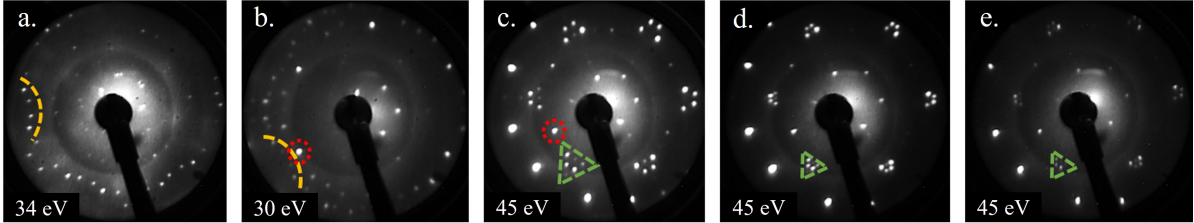


Figure S1: LEED patterns of Bi/Au(111). (a) Low-coverage $(\sqrt{37} \times \sqrt{37})R25.3^\circ$ phase. (b) Coexistence of the low- and high-coverage phases, as evidenced by the highlighted features (orange from panel a, red from panel c). (c) High-coverage $(P \times \sqrt{3})$ phase, one of the characteristic triangles is highlighted in green. (d) Near-monolayer coverage, with highlighted the shrinkage of the triangle of panel c. (e) Presumed multilayer after doubling the deposition time relative to panel d; no further change of the LEED pattern is observed besides a mild attenuation.

Deposition time (min)	LEED pattern	Estimated coverage (ML)	Literature coverage (ML)
8	No pattern	0.38	< 0.54
12	Figure S1a	0.57	0.63 – 0.81
17	Figure S1b	0.81	\sim 0.81
19	Figure S1c	0.91	\gtrsim 0.81
21	Figure S1d	1.00	0.81 – 5
41	Figure S1e	1.95	0.81 – 5

Table S1: Estimated coverages of corresponding to the LEED patterns in Figure S1 compared to the coverage indications provided by He et al. [23]. The estimates were calculated assigning the transition coverage of 0.81 ML to the system obtained with a deposition time of 17 min and assuming a constant sticking coefficient of Bi on the surface throughout deposition.

S2 The $(\sqrt{37} \times \sqrt{37})R25.3^\circ$ phase

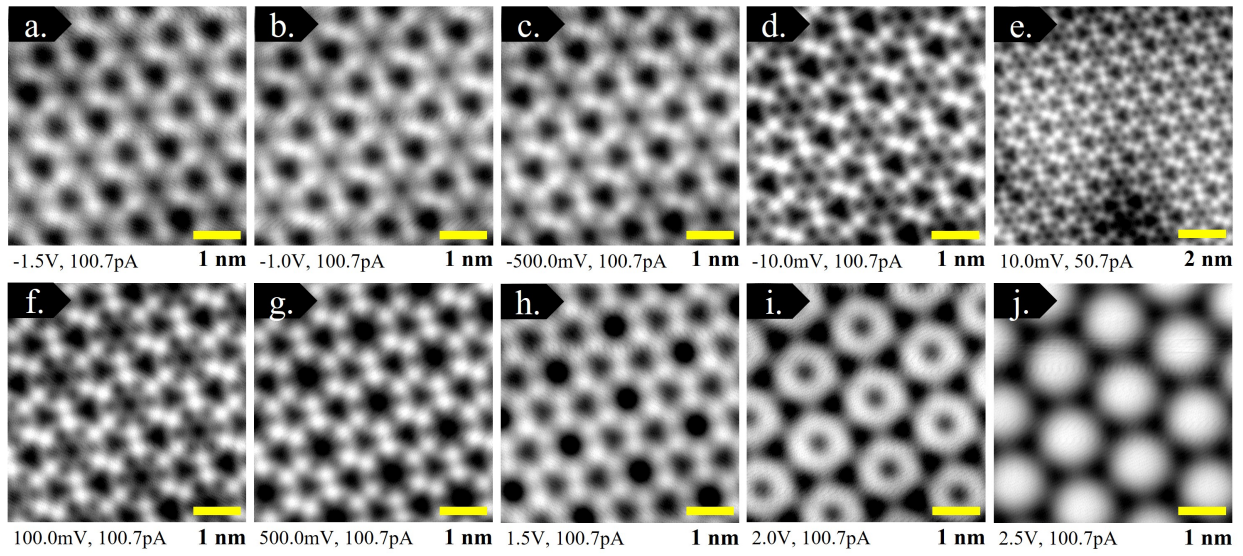


Figure S2: Low-Temperature STM images of the low-coverage Bi/Au(111) phase. This library matches the available literature [23, 21, 22] and expands it with images at higher tip-bias voltage (panels h-j).

S3 The $(P \times \sqrt{3})$ phase

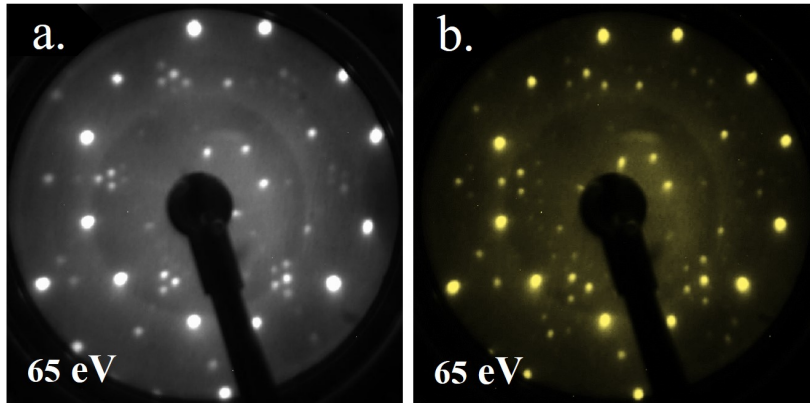


Figure S3: High-coverage, sub-monolayer Bi/Au(111). (a) LEED pattern at ≈ 1 ML. (b) LEED pattern at ≈ 0.9 ML. In Figure 3, the spots of panel b are superimposed on the image of panel a to facilitate the comparison.

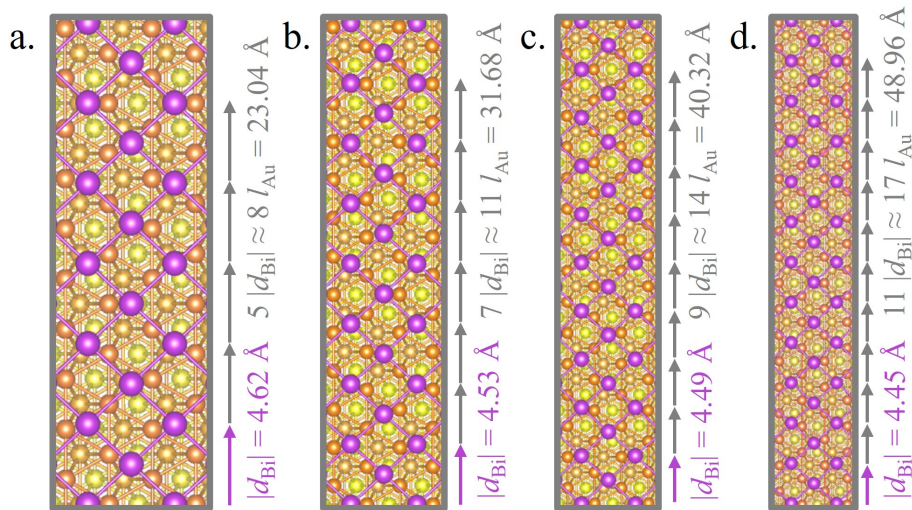


Figure S4: Structural models displaying the Bi moiré superstructures on Au(111) as the coverage increases (colour scheme defined in Figure 3b). Despite a decrease in the extension of the Bi unit cell perpendicular to the stripes (d_{Bi}), the moiré supercell grows along this lattice vector (b_{Bi}^*) by encompassing a larger number of unit cells. Panels a-d respectively correspond to the LEED patterns in Figure S1b-e.

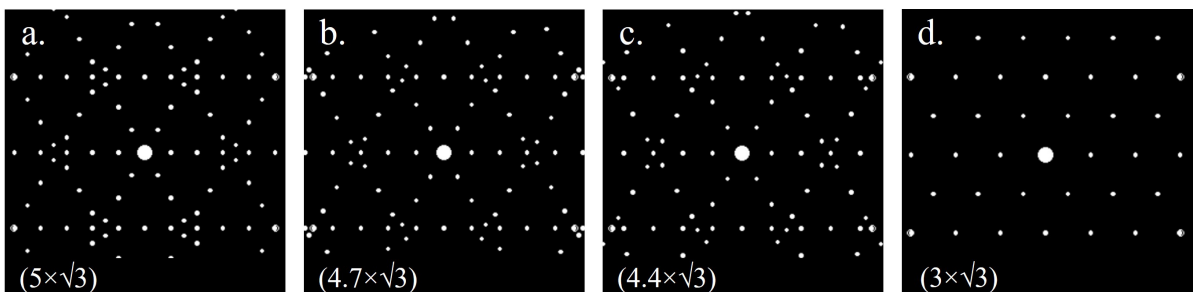


Figure S5: Kinematically simulated LEED patterns corresponding to the models described in the literature: (a-c) Kawakami et al. [22], (d) He et al. [23]. Notably, the patterns in panels b-d are incompatible with the experimental patterns reported in Figures 3 and S3.

S3.1 NIXSW principles

In NIXSW, a standing wave is created by directing a photon beam on a crystalline sample at normal incidence. When the photon energy is close to satisfying the Bragg condition, the interaction between incident and reflected waves leads to the formation of a standing wave, for which the range of appropriate photon energies is dictated by dynamical diffraction theory (DDT), as described by the Darwin reflectivity curve [47]. As the photon energies are scanned across the Darwin curve, a phase (ϕ) inversion in the standing wave [48], whereby its nodes and antinodes shift along the reflection direction by half of the crystal's spacing in this direction. Making use of the effect that the standing wave's amplitude has on the photoemission of adsorbed atoms, the photo-yield (Y) is derived from the modulation of the XPS signal's intensity for a chosen core level of the adsorbate (here, Bi $4f_{7/2}$) while the reflectivity (R) is directly measured. The photo-yield curve can then be described as [49]:

$$Y \propto 1 + R + 2f\sqrt{R} \cos(\phi - 2\pi p) \quad (1)$$

where f indicates the coherent function and p the coherent position. Known jointly as coherent parameters, they are derived from a fitting of the experimental photo-yield curve, which in turn requires fitting the reflectivity curve (Figure 4c).

As addressed in Section 3.2, standing waves can be induced relative to nonequivalent sets of planes (here, (111), $(\bar{1}11)$, and (200)). The sensitivity of XSW to the relative heights of the emitter atoms within each set of standing waves is then exploited in order to triangulate the positions of the adsorbate atoms. Relative to a generic (hkl) reflection, the coherent parameters (p_{hkl} , f_{hkl}) are calculated as a function of the position distribution (Z_{hkl}) of the adsorbate atoms above the closest [hkl] nodal plane of the standing wave [50]:

$$Z_{hkl} = \frac{1}{N} \sum_{j=1}^N \exp\left(2\pi i \frac{d_{j,hkl}}{h_{hkl}}\right) \quad (2)$$

$$p_{hkl} = \frac{1}{2\pi} \text{atan}\left(\frac{\text{I}(Z_{hkl})}{\text{R}(Z_{hkl})}\right) \quad (3)$$

$$f_{hkl} = \sqrt{\text{R}(Z_{hkl})^2 + \text{I}(Z_{hkl})^2} \quad (4)$$

where N is the number of adsorbate atoms, h_{hkl} is the planar spacing, and $d_{j,hkl}$ is the height of adsorbate atom j above the closest nodal plane. Assuming negligible relaxation of the substrate's surface layers, $d_{j,hkl}$ corresponds to the adsorption height only for the surface reflection (here, $d_{j,111}$) but will depend on it for any reflection not perpendicular to the surface direction (e.g. $(\bar{1}11)$ and (200)). We therefore constructed the structural models of the $(n \times \sqrt{3})A90^\circ$ Bi phases ($n = 5, 8, 11, 14$) as developed by means of STM and LEED (Section 3.2, and Figures S1, S4, S5, and S6) and simulated the coherent parameters of such structures on an ideal Au(111) surface. All high-symmetry adsorption sites were considered by manually reiterating the simulations, placing a "reference atom" in the desired site and constructing the rest of the Bi model from the geometrical considerations previously discussed (Figure S6). The average adsorption height was instead

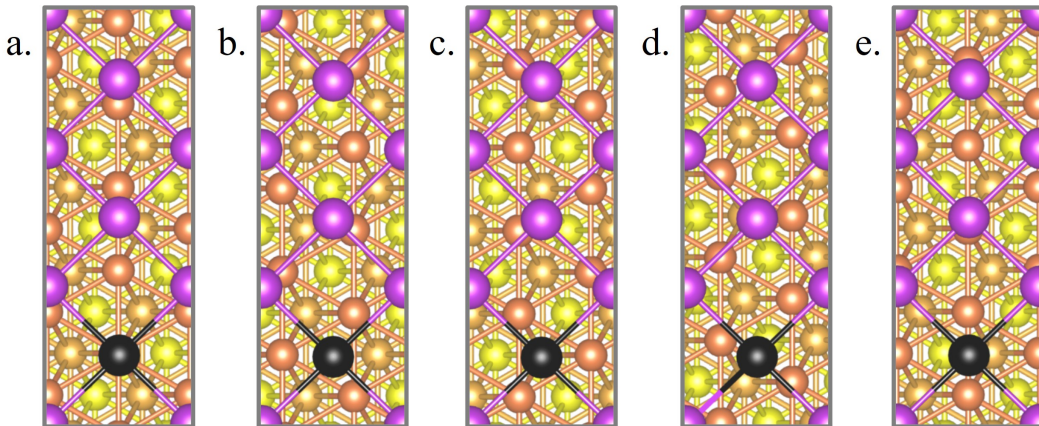


Figure S6: Structural models highlighting the unit cell of the $(5 \times \sqrt{3})A90^\circ$ moiré superstructure for different adsorption sites of the “reference atom” (black): (a) top, (b) fcc, (c) hcp, (d) “bridge 1” (equiv. “bridge 3”), (e) “bridge 2”. The colour scheme and adsorption sites are defined in Figure 3b-c respectively. Starting from the reference atom, all other Bi atoms are positioned based on the considerations made in Section 3.2 regarding Bi-Bi bond length, lattice angle and orientation relative to the substrate (cf. Figure 2d-e).

automatically changed in the analysis code as a rigid vertical shift of the Bi structure within an arbitrarily defined range, chosen as to include all physically reasonable values.

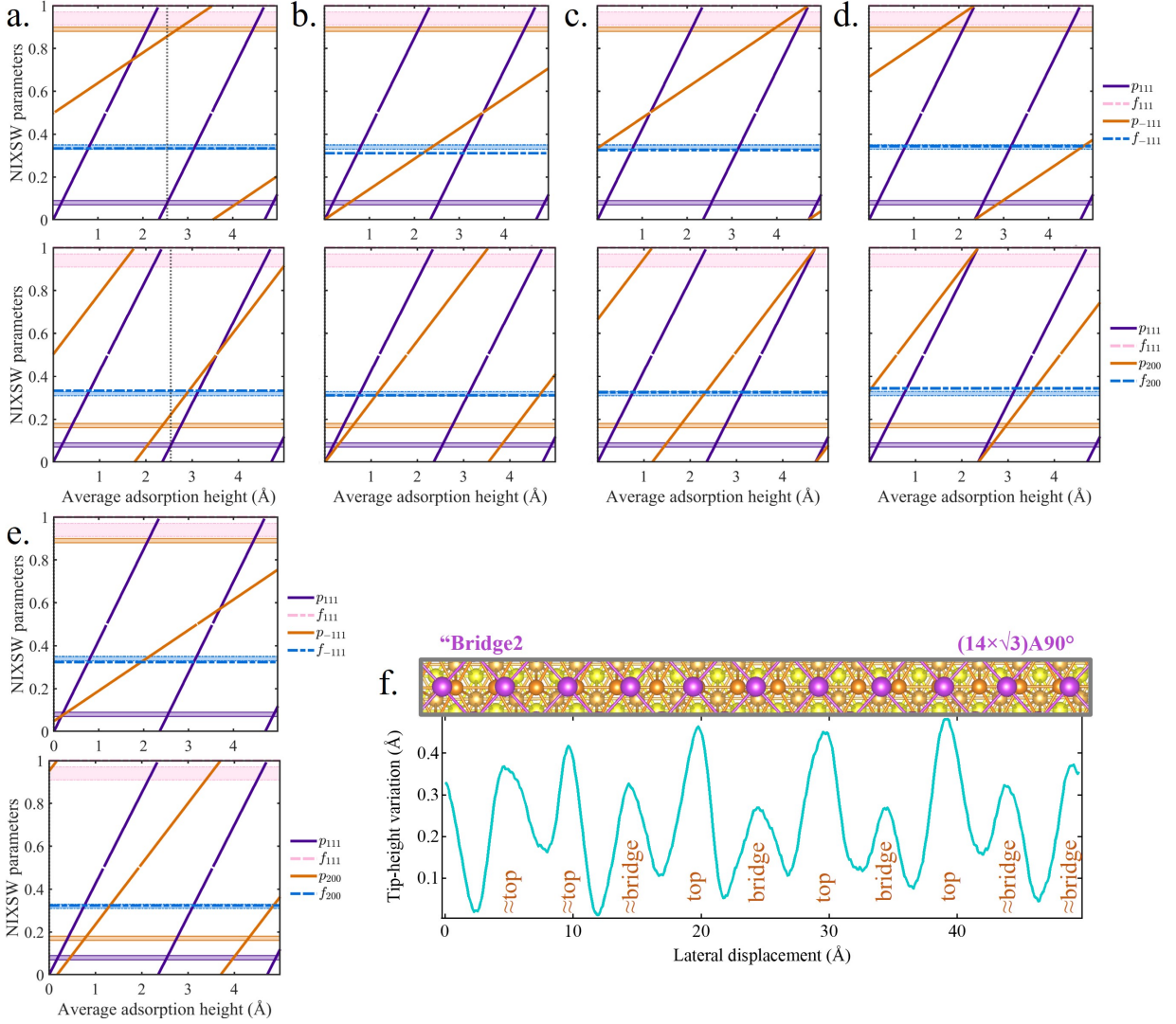


Figure S7: (a-e) Simulated coherent fraction and position plotted as a function of the adsorption height, referring to the ideal $(11 \times \sqrt{3})A90^\circ$ moiré superstructure. The colour-shaded areas indicate the value range measured experimentally for each parameter. The coherent values relative to the (111) reflection are compared to those relative to the $(\bar{1}\bar{1}\bar{1})$ reflection (top), and the (200) reflection (bottom). All high-symmetry adsorption sites are considered for the reference atom: (a) “bridge 1” (equivalent to “bridge 3”), (b) top, (c) fcc, (d) hcp, (e) “bridge 2”. (f) Graphical comparison of the adsorption sites in the “bridge 2” $(14 \times \sqrt{3})A90^\circ$ superstructure (above) with the line profile measured in STM (below). The approximate adsorption sites deduced from the model are written in orange, assuming the adsorption height in top sites to be larger than in bridge sites. The colour scheme of the structural model is defined in Figure 3b.

In Figure S7a-e are presented the NIXSW triangulation plots of an ideal $(11 \times \sqrt{3})A90^\circ$ moiré superstructure (i.e. flat and without any structural disorder) for different adsorption sites of the “reference atom” used to build the model (Figure S6). A match is found when the simulated parameters (lines) fall within the respective experimental ranges (horizontal bands) at a given adsorption height for all reflections (i.e. (111), $(\bar{1}\bar{1}\bar{1})$, (200)). Notably, none of the shown configurations satisfy this condition. The key element differentiating the “bridge 1” site (Figure S7a) is the presence of an adsorption height (2.54 Å, dotted vertical line) for which mild shifts of f_{111} , p_{111} , and p_{200} would lead to a match, as demonstrated by simulating thermal disorder through Gaussian deviations ($\sigma \leq 0.1$ Å) from the initial positions (Figure 4a-b). For all other high-symmetry adsorption sites, the discrepancy between simulated and experimental data is significantly larger (Figure S7b-e). This observation plays a fundamental role in refuting the possibility of “bridge 2” (and therefore top) adsorption sites, suggested by the STM height profile along the $[11\bar{2}]$ direction (Figure S7f).

S4 The multilayer

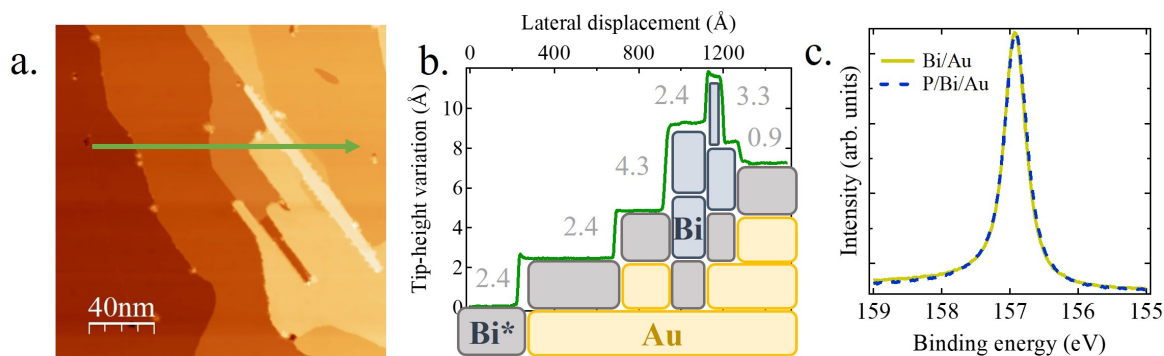


Figure S8: (a) STM image of a 2.14 ML Bi thin film on Au(111) ($V=1.00$ V, $I=10$ pA). The green arrow indicates the path of the height profile in panel b. (b) Comparison of the height profile from panel a with a matching layer stack, showing a rare single-layer Bi step and its attribution to the growing bilayer. The block heights are scaled so that the ratio Au:Bi*:Bi matches 2.35:2.54:3.28, representing the gold, first-layer Bi, and multilayer Bi single-step heights. In light grey are expressed the step heights (in Å). (c) Comparison of the HR-XPS Bi $4f_{7/2}$ core-level spectra before and after P deposition, measured at the I09 beamline (photon energy: 275 eV).

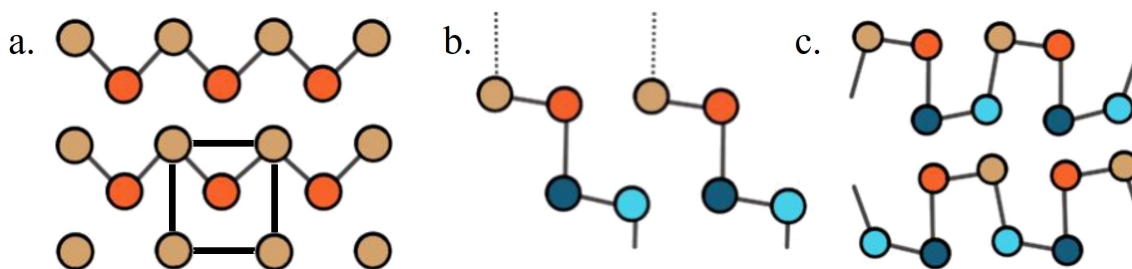


Figure S9: Structural representation of a Bi crystal. Covalent bonds are marked by solid lines, dangling bonds by dotted lines. (a) Top view ($[11\bar{0}]$ direction) of a single layer [44]. The unit cell is drawn with thick black lines. In monolayer Bi/Au(111) the inner atom (orange) is in the centre of the unit cell, which we attribute to the commensurate matching with the substrate's $[11\bar{2}]$ direction and an alignment with bridge adsorption sites. (b) Side view ($[11\bar{2}]$ direction) of the surface (brown and orange) and first subsurface (blue and cyan) layers of a Bi crystal [51], highlighting the presence of dangling bonds for half of the surface atoms. (c) Side view ($[11\bar{2}]$ direction) of four layers, rearranged as to saturate any dangling bonds by forming stacked bilayers [8].

References

- [1] E. Aktürk, O. Ü. Aktürk, and S. Ciraci, “Single and bilayer bismuthene: stability at high temperature and mechanical and electronic properties,” *Physical Review B*, vol. 94, no. 1, p. 014115, 2016.
- [2] C. R. Ast, J. Henk, A. Ernst, L. Moreschini, M. C. Falub, D. Pacilé, P. Bruno, K. Kern, and M. Grioni, “Giant spin splitting through surface alloying,” *Physical Review Letters*, vol. 98, no. 18, p. 186807, 2007.
- [3] S. Murakami, “Quantum spin hall effect and enhanced magnetic response by spin-orbit coupling,” *Physical Review Letters*, vol. 97, no. 23, pp. 1–4, 2006.
- [4] C. Sabater, D. Gosálbez-Martínez, J. Fernández-Rossier, J. G. Rodrigo, C. Untiedt, and J. J. Palacios, “Topologically protected quantum transport in locally exfoliated bismuth at room temperature,” *Physical Review Letters*, vol. 110, no. 17, p. 176802, 2013.
- [5] Z. Liu, C. X. Liu, Y. S. Wu, W. H. Duan, F. Liu, and J. Wu, “Stable nontrivial Z_2 topology in ultrathin Bi (111) films: a first-principles study,” *Physical Review Letters*, vol. 107, no. 13, p. 136805, 2011.
- [6] M. Wada, S. Murakami, F. Freimuth, and G. Bihlmayer, “Localized edge states in two-dimensional topological insulators: Ultrathin Bi films,” *Physical Review B - Condensed Matter and Materials Physics*, vol. 83, no. 12, pp. 2–5, 2011.
- [7] R. H. Miwa, T. M. Schmidt, and G. P. Srivastava, “Bi covered Si(111) surface revisited,” *Journal of Physics Condensed Matter*, vol. 15, no. 17, p. 2441–2447, 2003.
- [8] T. Nagao, J. T. Sadowski, M. Saito, S. Yaginuma, Y. Fujikawa, T. Kogure, T. Ohno, Y. Hasegawa, S. Hasegawa, and T. Sakurai, “Nanofilm allotrope and phase transformation of ultrathin Bi film on Si(111)- 7×7 ,” *Physical Review Letters*, vol. 93, no. 10, pp. 10–13, 2004.
- [9] J. Cui, M. Daboczi, M. Regue, Y.-C. Chin, K. Pagano, J. Zhang, M. Isaacs, G. Kerherve, A. Mornto, J. West, S. Gimenez, J.-S. Kim, and S. Eslava, “Two-Dimensional Bismuthene as a Functional Interlayer between BiVO_4 and NiFeOOH for Enhanced Oxygen-Evolution Photoanodes,” *Advanced Functional Materials*, vol. 32, p. 2207136, 2022.
- [10] Y. Liu, S. Benter, C. S. Ong, R. P. Maciel, A. Irish, O. Eriksson, A. Mikkelsen, and R. Timm, “A 2D Bismuth-Induced Honeycomb Surface Structure on GaAs(111),” *ACS Nano*, vol. 17, no. 5, pp. 5047–5058, 2023.
- [11] F. Reis, G. Li, L. Dudy, M. Bauernfeind, S. Glass, W. Hanke, R. Thomale, J. Schäfer, and R. Claessen, “Bismuthene on a SiC substrate: a candidate for a high-temperature quantum spin Hall material,” *Science*, vol. 357, pp. 287–290, 2017.
- [12] C. H. Hsu, Z. Q. Huang, F. C. Chuang, C. C. Kuo, Y. T. Liu, H. Lin, and A. Bansil, “The nontrivial electronic structure of Bi/Sb honeycombs on SiC(0001),” *New Journal of Physics*, vol. 17, p. 025005, 2015.
- [13] Y. Girard, C. Chacon, G. De Abreu, J. Lagoute, V. Repain, and S. Rousset, “Growth of Bi on Cu(111): alloying and dealloying transitions,” *Surface Science*, vol. 617, pp. 118–123, 2013.
- [14] C. Kato, Y. Aoki, and H. Hirayama, “Scanning tunneling microscopy of Bi-induced Ag(111) surface structures,” *Physical Review B - Condensed Matter and Materials Physics*, vol. 82, no. 16, p. 165407, 2010.
- [15] K. H. Zhang, I. M. McLeod, M. Lahti, K. Pussi, and V. R. Dhanak, “The evolution of the electronic structure at the Bi/Ag(111) interface studied using photoemission spectroscopy,” *Journal of Physics Condensed Matter*, vol. 24, no. 43, p. 435502, 2012.
- [16] K. H. Zhang, I. M. McLeod, Y. H. Lu, V. R. Dhanak, A. Matilainen, M. Lahti, K. Pussi, R. G. Egdell, X. S. Wang, A. T. Wee, and W. Chen, “Observation of a surface alloying-to-dealloying transition during growth of Bi on Ag(111),” *Physical Review B - Condensed Matter and Materials Physics*, vol. 83, no. 23, p. 235418, 2011.
- [17] C.-h. Chen, K. D. Kepler, A. A. Gewirth, B. M. Ocko, and J. Wang, “Electrodeposited Bismuth Monolayers on Au(111) Electrodes: Comparison of Surface X-ray Scattering, Scanning Tunneling Microscopy, and Atomic Force Microscopy Lattice Structures,” *Journal of Physical Chemistry*, vol. 97, pp. 7290–7294, 1993.

- [18] K. Tamura, J. X. Wang, R. R. Adžic, and B. M. Ocko, “Kinetics of Monolayer Bi Electrodeposition on Au(111): Surface X-ray Scattering and Current Transients,” *Journal of Physical Chemistry B*, vol. 108, no. 6, pp. 1992–1998, 2004.
- [19] Y. C. Fu, Y. Z. Su, H. M. Zhang, J. W. Yan, Z. X. Xie, and B. W. Mao, “An in situ scanning tunneling microscopic study of electrodeposition of bismuth on Au(1 1 1) in a 1-butyl-3-methylimidazolium tetrafluoroborate ionic liquid: Precursor adsorption and underpotential deposition,” *Electrochimica Acta*, vol. 55, no. 27, pp. 8105–8110, 2010.
- [20] M. Nakamura, N. Sato, N. Hoshi, and O. Sakata, “Catalytically active structure of Bi deposited on a Au(111) electrode for the hydrogen peroxide reduction reaction,” *Langmuir*, vol. 26, no. 7, pp. 4590–4593, 2010.
- [21] J. H. Jeon, K. H. Chung, H. Kim, and S. J. Kahng, “Corner hole adatom stacking fault structure of Bi on Au(1 1 1),” *Surface Science*, vol. 603, no. 1, pp. 145–150, 2009.
- [22] N. Kawakami, C. L. Lin, K. Kawahara, M. Kawai, R. Arafune, and N. Takagi, “Structural evolution of Bi thin films on Au(111) revealed by scanning tunneling microscopy,” *Physical Review B*, vol. 96, no. 20, p. 205402, 2017.
- [23] B. He, G. Tian, J. Gou, B. Liu, K. Shen, Q. Tian, Z. Yu, F. Song, H. Xie, Y. Gao, Y. Lu, K. Wu, L. Chen, and H. Huang, “Structural and electronic properties of atomically thin bismuth on Au(111),” *Surface Science*, vol. 679, pp. 147–153, 2019.
- [24] G. Tian, Y. Shen, B. He, Z. Yu, F. Song, Y. Lu, P. Wang, Y. Gao, and H. Huang, “Effects of monolayer Bi on the self-assembly of DBBA on Au(111),” *Surface Science*, vol. 665, no. 111, pp. 89–95, 2017.
- [25] F. Donati, S. Rusponi, S. Stepanow, C. Wäckerlin, A. Singha, L. Persichetti, R. Baltic, K. Diller, F. Patthey, E. Fernandes, J. Dreiser, Šljivančanin, K. Kummer, C. Nistor, P. Gambardella, and H. Brune, “Magnetic remanence in single atoms,” *Science*, vol. 352, no. 6283, pp. 318–321, 2016.
- [26] L. Grossmann, B. T. King, S. Reichlmaier, N. Hartmann, J. Rosen, W. M. Heckl, J. Björk, and M. Lackinger, “On-surface photopolymerization of two-dimensional polymers ordered on the mesoscale,” *Nature Chemistry*, vol. 13, no. 8, pp. 730–736, 2021.
- [27] T. L. Lee and D. A. Duncan, “A Two-Color Beamline for Electron Spectroscopies at Diamond Light Source,” *Synchrotron Radiation News*, vol. 31, no. 4, pp. 16–22, 2018.
- [28] See Supplemental Material at <https://thelinkofthepaper.com> for the coverage calibration, the details of the NIXSW analysis, and other supporting figures.
- [29] G. H. Major, N. Fairley, P. M. A. Sherwood, M. R. Linford, J. Terry, V. Fernandez, and K. Artyushkova, “Practical guide for curve fitting in X-ray photoelectron spectroscopy,” *Journal of Vacuum Science Technology A*, vol. 38, no. 6, p. 061203, 2020.
- [30] M. H. Engelhard, D. R. Baer, A. Herrera-Gomez, and P. M. A. Sherwood, “Introductory guide to backgrounds in XPS spectra and their impact on determining peak intensities,” *Journal of Vacuum Science Technology A*, vol. 38, no. 6, p. 063203, 2020.
- [31] A. Riss, “Spmimage tycoon: Organize and analyze scanning probe microscopy data,” *Journal of Open Source Software*, vol. 7, no. 77, p. 4644, 2022.
- [32] I. Horcas, R. Fernández, J. M. Gómez-Rodríguez, J. Colchero, J. Gómez-Herrero, and A. M. Baro, “WSXM: A software for scanning probe microscopy and a tool for nanotechnology,” *Review of Scientific Instruments*, vol. 78, no. 1, p. 013705, 2007.
- [33] K. Hermann and M. A. V. Hove, “Software utility LEEDpat (version 4.2),” *Berlin/Hong Kong*, 2015.
- [34] K. Momma and F. Izumi, “VESTA3 for three-dimensional visualization of crystal, volumetric and morphology data,” *Journal of Applied Crystallography*, vol. 44, no. 6, pp. 1272–1276, 2011.
- [35] P. Hohenberg and W. Kohn, “Inhomogeneous Electron Gas,” *Physical Review*, vol. 136, no. 3B, p. B864, 1964.
- [36] P. Giannozzi, S. Baroni, N. Bonini, M. Calandra, R. Car, C. Cavazzoni, D. Ceresoli, G. L. Chiarotti, M. Cococcioni, I. Dabo, A. Dal Corso, S. De Gironcoli, S. Fabris, G. Fratesi, R. Gebauer, U. Gerstmann, C. Gougoussis, A. Kokalj, M. Lazzeri, L. Martin-Samos, N. Marzari, F. Mauri, R. Mazzarello, S. Paolini, A. Pasquarello, L. Paulatto, C. Sbraccia, S. Scandolo, G. Sclauzero, A. P. Seitsonen, A. Smogunov,

- P. Umari, and R. M. Wentzcovitch, “QUANTUM ESPRESSO: A modular and open-source software project for quantum simulations of materials,” *Journal of Physics Condensed Matter*, vol. 21, no. 39, 2009.
- [37] G. Kresse and J. Furthmüller, “Efficient iterative schemes for ab initio total-energy calculations using a plane-wave basis set,” *Physical Review B*, vol. 54, no. 16, p. 11169, 1996.
- [38] J. P. Perdew, K. Burke, and M. Ernzerhof, “Generalized Gradient Approximation Made Simple,” *Physical Review Letters*, vol. 77, no. 18, pp. 3865–3868, 1996.
- [39] A. Maeland and T. B. Flanagan, “Lattice spacings of gold-palladium alloys,” *Canadian Journal of Physics*, vol. 42, pp. 2364–2366, 1964.
- [40] F. Pan, B. Peerless, and S. Dehnen, “Bismuth-Based Metal Clusters From Molecular Aesthetics to Contemporary Materials Science,” *Accounts of Chemical Research*, vol. 56, no. 9, pp. 1018–1030, 2023.
- [41] J. Zegenhagen and A. Kazimirov, *The X-Ray Standing Wave Technique*. World Scientific, 2013.
- [42] B. P. Klein, M. A. Stoodley, D. B. Morgan, L. A. Rochford, L. B. Williams, P. T. Ryan, L. Sattler, S. M. Weber, G. Hilt, T. J. Liddy, T. L. Lee, R. J. Maurer, and D. A. Duncan, “Probing the role of surface termination in the adsorption of azulene on copper,” *Nanoscale*, vol. 16, pp. 5802–5812, 2024.
- [43] J. F. Moulder, W. F. Stickle, P. E. Sobol, and K. D. Bomben, *Handbook of X-ray Photoelectron Spectroscopy*. Perkin-Elmer Corporation, 1992.
- [44] G. Bian, X. Wang, T. Miller, T. C. Chiang, P. J. Kowalczyk, O. Mahapatra, and S. A. Brown, “First-principles and spectroscopic studies of Bi(110) films: Thickness-dependent Dirac modes and property oscillations,” *Physical Review B - Condensed Matter and Materials Physics*, vol. 90, no. 19, p. 195409, 2014.
- [45] F. He, E. S. Walker, and Y. Zhou, “Phase transition in epitaxial bismuth nanofilms,” *Applied Physics Letters*, vol. 117, p. 073103, 2020.
- [46] M. Jankowski, D. Kamiński, K. Vergeer, M. Miroló, F. Carla, G. Rijnders, and T. R. Bollmann, “Controlling the growth of Bi(110) and Bi(111) films on an insulating substrate,” *Nanotechnology*, vol. 28, no. 15, 2017.
- [47] B. W. Batterman, “Effect of dynamical diffraction in x-ray fluorescence scattering,” *Physical Review*, vol. 133, no. 3A, pp. A759–A764, 1964.
- [48] J. Als-Nielsen and D. McMorrow, *Elements of Modern X-ray Physics*. Wiley, 2011.
- [49] D. P. Woodruff, “Surface structure determination using x-ray standing waves,” *Reports on Progress in Physics*, vol. 68, no. 4, pp. 743–798, 2005.
- [50] J. Zegenhagen, “Surface structure determination with X-ray standing waves,” *Surface Science Reports*, vol. 18, pp. 199–271, 1993.
- [51] P. Hofmann, “The surfaces of bismuth: Structural and electronic properties,” *Progress in Surface Science*, vol. 81, no. 5, pp. 191–245, 2006.